



Die Grenzen der
Chemie neu ausloten?
It takes
#HumanChemistry

Wir suchen kreative Chemikerinnen und Chemiker,
die mit uns gemeinsam neue Wege gehen wollen –
mit Fachwissen, Unternehmertum und Kreativität für
innovative Lösungen. Informieren Sie sich unter:

[evonik.de/karriere](https://www.evonik.de/karriere)

Mechanical Characterization of Compact Rolled-up Microtubes Using In Situ Scanning Electron Microscopy Nanoindentation and Finite Element Analysis

Somayeh Moradi,* Nathanael Jöhrmann, Dmitriy D. Karnaushenko,*
Uwe Zschenderlein, Daniil Karnaushenko, Bernhard Wunderle, and Oliver G. Schmidt*

Self-assembled Swiss-roll microstructures (SRMs) are widely explored to build up microelectronic devices such as capacitors, transistors, or inductors as well as sensors and lab-in-a-tube systems. These devices often need to be transferred to a special position on a microchip or printed circuit board for the final application. Such a device transfer is typically conducted by a pick-and-place process exerting enormous mechanical loads onto the 3D components that may cause catastrophic failure of the device. Herein, the mechanical deformation behavior of SRMs using experiments and simulations is investigated. SRMs using in situ scanning electron microscopy (SEM) combined with nanoindentation are characterized. This allows us to mimic and characterize mechanical loads as they occur in a pick-and-place process. The deformation response of SRMs depends on three geometrical factors, i.e., the number of windings, compactness of consecutive windings, and inner diameter of the microtube. Nonlinear finite element analysis (FEA) showing good agreement with experiments is performed. It is believed that the insights into the mechanical loading of 3D self-assembled architectures will lead to novel techniques suitable for a new generation of pick-and-place machines operating at the microscale.

assembly techniques also become more challenging.^[3] Tiny components can be easily damaged due to excessive mechanical loads applied to fragile 3D architectures during the standard pick-and-place processes.^[4] Therefore, extensive mechanical evaluation of these structures is required to understand and prevent damages, and increase assembly yield and board-level reliability. A deep understanding of their mechanical behavior will lead to the right choice of materials, proper design parameters, appropriate manufacturing, and integration processes.


Rolled-up nanotechnology has offered an advanced platform based on strain engineering to deterministically rearrange 2D nanomembranes into 3D structures realizing complex 3D micro- and nanoelectronic as well as optical and microfluidic components.^[5–9] Over the past decades SRM-based electronic devices with outstanding performance such as SRM capacitors,^[10–14] inductors,^[15–19] transistors,^[20–22] sensors,^[23,24] diodes,^[25] and antennas^[26] have been successfully demonstrated.

The SRM devices are by nature thin-film structures that are self-assembled into 3D microarchitectures. There can be a huge ratio between device dimension and wall thickness, which can reach values >1000, making these structures mechanically susceptible to vanishingly small loads, such as surface tension of liquids, touch with tweezers, or simple air flow.

1. Introduction

The next-generation of electronic circuits will include manufacturing in 3D space.^[1,2] 3D circuits and devices will open up possibilities for further miniaturization and achieve geometries inaccessible so far for planar technologies. However, with the growing complexity and continuous miniaturization, pick-and-place

S. Moradi, N. Jöhrmann, Dr. U. Zschenderlein, Prof. B. Wunderle, Prof. O. G. Schmidt
Center for Materials
Architectures and Integration of Nanomembranes (MAIN)
Chemnitz University of Technology
Rosenberg Str. 6, 09126 Chemnitz, Germany
E-mail: s.moradi@ifw-dresden.de; o.schmidt@ifw-dresden.de

 The ORCID identification number(s) for the author(s) of this article can be found under <https://doi.org/10.1002/adem.202100412>.

© 2021 The Authors. Advanced Engineering Materials published by Wiley-VCH GmbH. This is an open access article under the terms of the Creative Commons Attribution License, which permits use, distribution and reproduction in any medium, provided the original work is properly cited.

DOI: 10.1002/adem.202100412

S. Moradi, Dr. D. D. Karnaushenko, Dr. D. Karnaushenko, Prof. O. G. Schmidt
Institute for Integrative Nanosciences
Leibniz IFW Dresden
Helmholtzstraße 20, 01069 Dresden, Germany
E-mail: dmitriy.karnaushenko@ifw-dresden.de

S. Moradi, Prof. O. G. Schmidt
Material Systems for Nanoelectronics
Chemnitz University of Technology
Reichenhainer Straße 70, 09107 Chemnitz, Germany

N. Jöhrmann, Dr. U. Zschenderlein, Prof. B. Wunderle
Materials and Reliability of Microsystems
Chemnitz University of Technology
Reichenhainer Straße 70, 09107 Chemnitz, Germany

Every year more than a trillion surface mount technology (SMT) capacitors are produced^[27,28] which must be positioned by pick-and-place machines into mobile phones, laptops, and onto printed circuit boards (PCB). The conventional pick-and-place process consists of picking up the electronic component from a feeder using a vacuum nozzle and transporting it to the specific location on the circuit board. The forces applied by the pick-and-place nozzle must be carefully monitored and limited as any uncontrolled pick and place with greater force can lead to catastrophic damages.^[29–33] For example, a maximum vertical force of ≈ 1.5 N for conventional complementary metal–oxide–semiconductor (CMOS) chips and a maximum force of ≈ 0.8 N for 50 μm -thick photosensitive chips are allowed during pick-and-place operations.^[34] The risk of component cracking can be controlled by selecting the proper setup and right pick-and-place head of the pick-and-place machine. Depending on the size, shape, and weight of the component, different nozzles such as chip or gripper nozzles can be used. For picking and placing SMT components, low-force nozzle options with flat surface and a size slightly smaller than the component body are recommended.^[31,33–35] For instance, for the standard flat chip 0402 with a length of 1000 μm and a width of 500 μm , a standard nozzle with an inner diameter of 400 μm and an outer diameter of 700–1000 μm is used.^[36] However, pick-and-place operation on microscale 3D components such as SRMs, which are extremely small, should be performed with high-resolution vision systems^[37] and possibly curved nozzles. Despite a large amount of research and multifunctionalities of SRMs covering various technological disciplines, only a few attempts to study the mechanical behavior of rolled-up architectures have been reported. For instance, Zhang et al. evaluated mechanical properties of SRMs using nanomanipulation in a scanning electron microscope (SEM).^[38] Müller et al. have reported mechanical deformation of SRMs using an ex situ nanoindentation technique.^[39] However, there is no systematic study of the mechanical behavior of SRMs determining the basic load requirements for a successful pick-and-place operation. Comprehensive mechanical characterization of individual SRMs can lead to more intelligent and relevant design of these architectures allowing to withstand the significant mechanical forces applied during standard assembly processes.

Here, we analyze the mechanical stability and deformation behavior of the SRMs from both experimental and computational perspectives. We mechanically characterize SRMs using an in situ SEM depth-sensing nanoindentation system. Using such a technique provides accurate load–displacement measurements and allows to observe real-time deformations and defect dynamics of the SRMs under different loading conditions. Specifically, the impact of key geometric characteristics on the mechanical deformation of SRMs such as the number of microtube windings (N_w), compactness level of consecutive windings, and inner diameter of the microtube (D_{inn}) are precisely evaluated. These evaluations provide useful guidelines to develop mechanically more reliable SRM devices for future electronic assembly techniques. In addition, comprehensive nonlinear finite element analysis (FEA) is applied to predict and compare the mechanical behavior of SRMs. Accurately determining mechanical behavior of SRMs is helpful not only to develop a basis for structural design and optimization of fabrication parameters but also to provide key process parameters for the new generation of pick-and-place machines capable of supporting assembly of a wider range of 3D component dimensions and geometries.

2. Fabrication of Self-Assembled SRMs

To create SRMs, we applied the dry fluorocarbon (FC) layer-assisted and heat-induced rolling method^[40] which relies on the adhesion–delamination phenomenon at the interface of different materials. It uses hydrophobicity of FC polymers and the thermal expansion difference of polymers and inorganic materials upon heat treatment. This technique is able to control the winding interfacial defects (voids and looseness) and create largely interfacial defect-free multiwinding SRMs. Such a dry release method minimizes the complexity of the fabrication process by eliminating the sacrificial layer etching step during the self-assembly process.

As shown in **Figure 1a**, the fabrication process starts with dip coating of the FC layer on a Si substrate. To improve the adhesion between the FC layer and the substrate, we heat the sample to 120 °C for 2 min. Afterward, the strained layers are deposited by electron beam evaporation at a low-temperature condition (<60 °C). After the deposition process, the samples are heated on a typical hotplate between 140 and 160 °C. Large thermal stress builds up at the inorganic nanomembrane/FC interface due to the large difference in the coefficients of thermal expansion (CTE) of the polymer FC layer and inorganic layer upon heating. This stress separates the nanomembrane from the polymer FC layer and rolls it into an ultracompact SRM (mechanism I). The FC layer not only provides an antiadhesion surface for the deposited layers, but also has a very low adhesion to the substrate surface, itself. Therefore, based on mechanism II, the FC polymer layer can separate from the substrate and (partially or totally) roll up with the strained nanomembrane.^[40] The SEM images in **Figure 1b** show the planar strained nanomembranes comprising a Ti/Cr bilayer and the SRMs released by a 200 nm-thick FC polymer layer upon heating on a hotplate at 140 °C for a few minutes. Cross-sectional SEM images (**Figure 1c**) reveal the effectiveness of the dry FC-assisted rolling mechanism for creating highly symmetric and compact SRMs made of different material combinations and winding numbers.

3. Mechanical Testing

Nanoindentation methods are well suited to probe the mechanical loading during a pick-and-place process.^[41–48] In nanoindentation tests, a miniature and highly sensitive hardness tester, the nanoindenter, is used for the load and displacement measurements. The force needed to press the indenter into a test object is continuously recorded as a function of the depth of indentation. The mechanical fingerprint of the materials behavior to the contact deformation can be provided by the nanoindentation load–displacement curves.^[47] Most of the nanoindentation data such as the load–displacement curves are collected ex situ and the indentation images are captured postmortem. In these systems, the deformation behavior of the tested micro- or nanostructures has to be interpreted based on the load–displacement responses and the indentations. Using a nanoindentation system inside a SEM is more informative and provides real-time indentation-induced structural deformation data.^[48]

With regard to the geometry and structural dimensions of SRMs studied in this work (e.g., inner diameter of 3–11 μm) and the typical chip nozzle for a standard pick-and-place

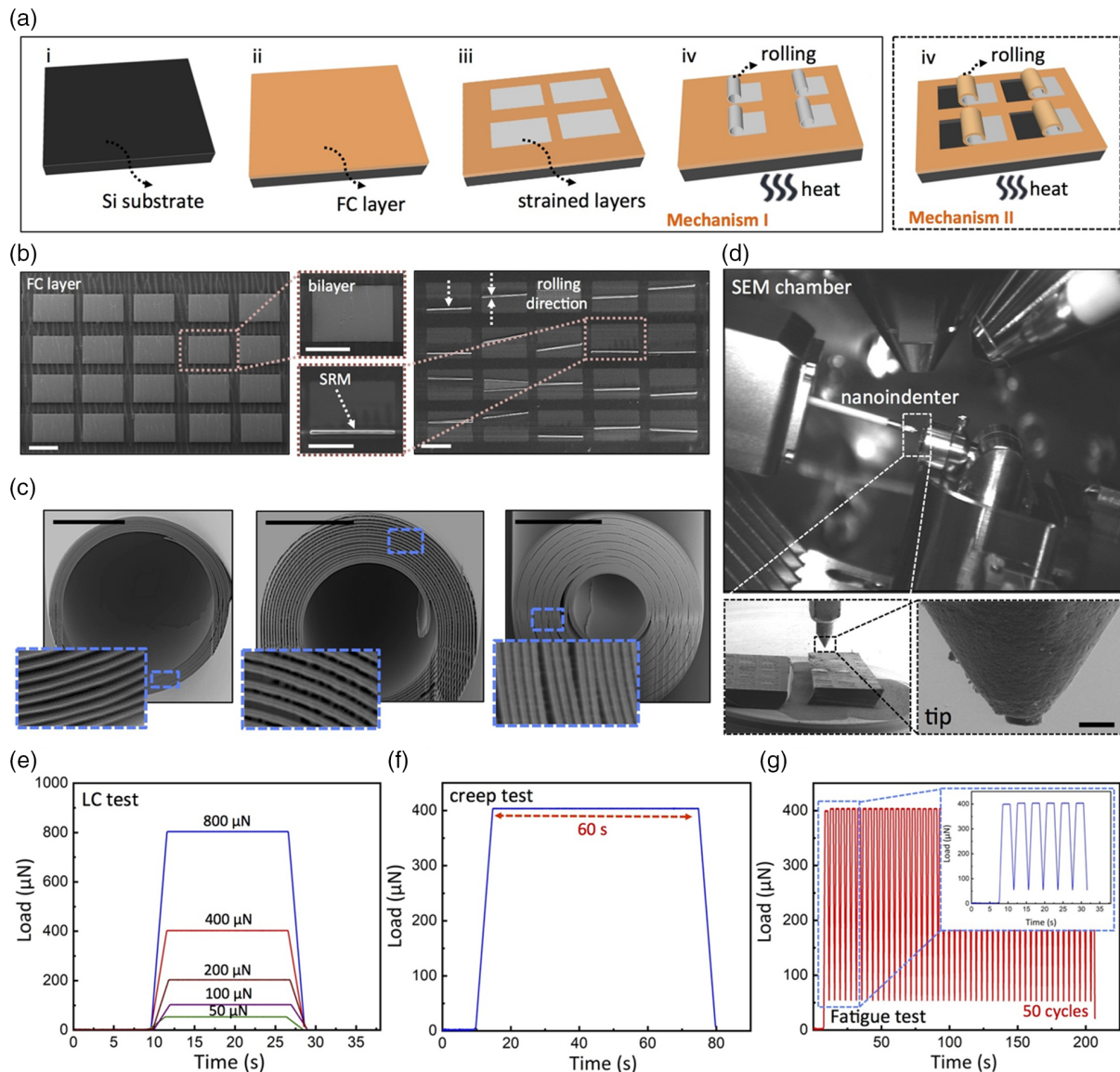


Figure 1. Mechanical characterization of compact SRMs fabricated by FC-assisted rolling technique. a) Schematic illustration of the dry FC-assisted rolling fabrication process. b) SEM images of the planar nanomembranes comprising of the bilayer of Ti/Cr and the SRMs detached by a 200 nm-thick FC layer upon heat treatment at 140 °C. Scale bars are 200 μm . c) Cross-sectional SEM images of the compact SRMs made of different material combinations and windings number. Scale bars are 5 μm . d) In situ SEM nanoindentation system equipped with a 5 μm diameter flat cylindrical tip. Scale bar is 5 μm . e–g) Nanoindentation loading–unloading conditions including: e) LC test at different maximal applied forces with different loading rates, f) creep test at maximum load of 400 μN and holding time of 60 s, and g) cyclic test at maximal force of 400 μN for 50 cycles.

operation, we used an in situ nanoindentation system equipped with a 5 μm diameter flat cylindrical punch (Figure 1d). The capability to perform indentation tests over a wide range of loads from μN to mN and accurately position the indenter on the microscale objects enables us to estimate the critical forces for the pick-and-place of SRMs.

Typical load–displacement curves were obtained in the load-controlled (LC) mode. Considering the speed at which the pick-and-place head would move toward and out of SRMs, different loading rates were used. For instance, the loading rate

for a peak load of 400 μN was set to 200 $\mu\text{N s}^{-1}$. A creep test was also performed to check whether the mechanical stability of the SRMs is sensitive to possible hold times during the (manual) pick-and-place operation. The effect of creep was studied at 400 μN with a hold period of 60 s at the maximum load. Moreover, cyclic nanoindentation tests^[49,50] were performed to determine the fatigue behavior of the rolled-up microtubes. Some of the indentation conditions for the typical LC, time-dependent, and cycling tests are shown in Figure 1e–g.

4. Numerical Simulations

FEA was performed by a commercial software tool ANSYS 17.2 Academics. Accurate replication of the experimental testing conditions in the models gives us the opportunity to easily vary the parameters or experimental conditions. This allows to explore different scenarios and provide guidelines for the proper design of further indentation experiments. Moreover, the computational models can be used to determine quantities that cannot be easily measured experimentally.

In the simulation analysis we assumed the compact SRM to be a hollow cylindrical structure. To replicate the experimental conditions for the bilayer microtubes, the thickness of a single winding was set to 0.035 μm . The total wall thickness of a microtube with a specific number of windings is given by

$$t_{\text{wall}} = N_w \times 0.035 \quad (1)$$

where t_{wall} is the overall thickness of the microtube wall and N_w is the number of windings. A bilinear isotropic metal plasticity model and a titanium alloy for the microtube material were selected for our numerical designs. Similar to the experiments the microtubes are indented by a 5 μm diameter flat cylindrical incompressible object. The mechanical behavior of the microtubes upon application and subsequent removal of the displacement loads was examined. The models were used to determine the magnitude and distribution of deformation, stress, and strain in the microtubes.

5. Results and Discussions

5.1. Effect of Number of Windings

To investigate the effect of N_w on the mechanical behavior of SRMs, we fabricated SRMs consisting of Ti (15 nm)/Cr (20 nm) with $N_w = 5, 15,$ and 50 keeping $D_{\text{inn}} = \approx 3 \mu\text{m}$ constant (see Experimental Section). The SRMs were mechanically indented on a Si substrate and load–displacement curves were obtained under different loading conditions. The deformation behavior of the compact SRMs with different number of windings under different loading conditions is shown in **Figure 2a–f**. **Figure 2a** compares the load–displacement curves obtained in the LC mode at a maximum load of 400 μN . It is observed that the penetration depth of the nanoindentation tip for the SRM with N_w of 5 is around $\approx 1050 \text{ nm}$, which is considerably higher than the displacement values of ≈ 130 and $\approx 35 \text{ nm}$ for the 15- and 50-winding SRMs, respectively. The stiffness of the SRM, S , which is determined as the slope of the unloading curve at the maximum loading point, increases dramatically from ≈ 1.8 to $\approx 33 \text{ kN m}^{-1}$ when N_w increases from 5 to 50. Moreover, the pop-in event as a sudden displacement excursion in the loading section of the load–displacement curve reflects the permanent damage of this SRM below the nanoindenter tip.^[42–44] Inset SEM images reveal the damage of the five-winding SRM after applying the maximum load of 400 μN . In contrast, no obvious abnormal events are observed in the load–displacement curves of the 15- and 50-winding SRMs, which confirms their mechanical stability under this loading condition. For less windings (e.g., five), the exact position of the nanomembrane edge might also

play a role and should be considered to fully understand the mechanical behavior of the SRM (more detail in **Figure S1**, Supporting Information).

To further analyze the effect of N_w on the mechanical deformation of the SRMs, we continued the LC mode indentation tests on the thicker and more stable 15- and 50-winding SRMs at different applied forces ranging from a maximum load of 200 to 3200 μN , as shown in **Figure 2b**. The figure clearly reveals that the displacement values for the 50-winding SRM under the same loading conditions is much lower compared with the 15-winding SRM, which indicates higher mechanical stiffness of the thick-walled 50-winding SRM. At the maximum load of 3200 μN , the displacement of the 15-winding SRM is $\approx 1750 \text{ nm}$ and it undergoes around $\approx 70\%$ irreversible deformation. In contrast, the 50-winding SRM only experiences a displacement of $\approx 400 \text{ nm}$ and permanent deformation of around $\approx 48\%$ when it is subjected to this high load. Moreover, it is apparent that the load–displacement plot of the 15-winding SRM at the maximum load of 3200 μN has deviated from the ideal shape and some abnormal phenomena such as pop-ins in the loading sequence appear. As the SEM inset image clearly shows, these abnormal events are related to the permanent damage of the SRM below the indenter tip. However, as no mechanical damage was observed during the indentation of the 50-winding SRM and its load–displacement curve does not contain any abnormal shapes, it can be concluded that this thick-walled SRM is mechanically stable even under the severe loading situation.

Accurately controlling the applied loads in the nanoindentation system allows for sensitive creep displacement measurements. To evaluate the time-dependent behavior, we applied a 60 s hold segment at the maximum load of 400 μN . Typical nanoindentation load–displacement plots for the 15- and 50-winding SRMs with the peak indentation load-holding segment are shown in **Figure 2c**. Based on the creep load–displacement plots, the thicker SRM with 50 windings shows a creep depth of around $\approx 10 \text{ nm}$, while for the 15-winding SRM, creep deformation of approximately $\approx 90 \text{ nm}$ is observed. These nanoindentation creep results demonstrate that the thick-walled SRM undergoes lower creep deformation than the thinner ones.

To evaluate the fatigue behavior of SRMs, we used nanoindentation by applying cyclic loading at the same location on the SRM. Cyclic indentation tests were conducted under a LC mode in the load range from 50 to 400 μN for various cycling numbers. **Figure 2d** shows the load–displacement curves of cyclic indentation for maximum loading–unloading cycles of 50 and 650 for the 50- and 15-winding SRMs, respectively. The indentation displacement continues to increase for the full duration of the tests for both SRMs. Based on the cyclic data, a maximum displacement of around $\approx 70 \text{ nm}$ is measured for the 50-winding SRM after 50 indentation cycles compared with a maximum penetration depth of around $\approx 200 \text{ nm}$ for the 15-winding SRM. By increasing the number of cycles to 650 for the 15-winding SRM, the displacement of the indenter reaches around $\approx 570 \text{ nm}$. **Figure 2e,f** shows that except for the larger plastic deformation after the first cycle, the plastic displacement of each cycle slightly decreases and saturates. No fatigue failures occurred for the 15-winding SRM after 650 cycles.

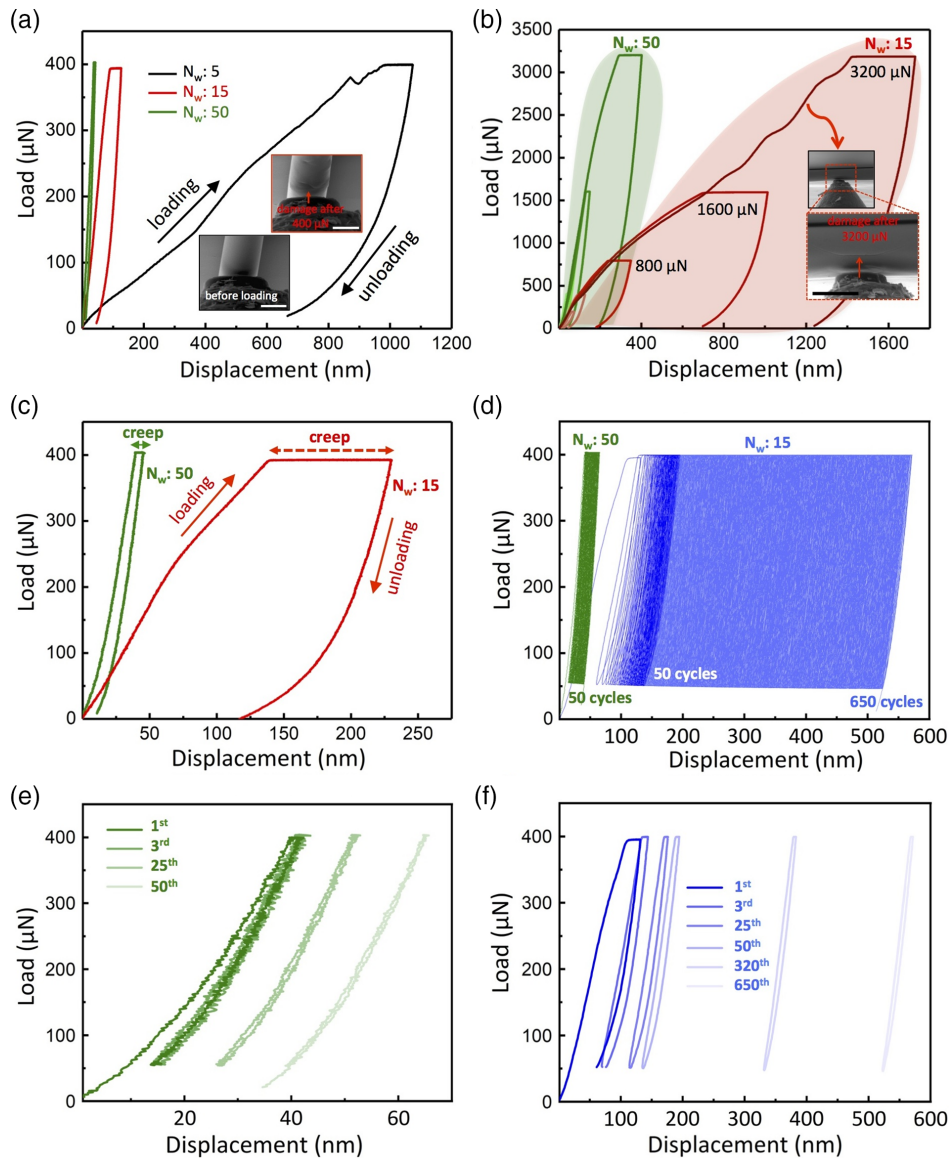


Figure 2. Effect of winding number on mechanical behavior of SRMs. a) Load–displacement curves of the SRMs with different winding numbers of 5, 15, and 50 at maximum load of $400 \mu\text{N}$ obtained by LC tests. Inset: SEM images of five-winding SRM before and after applying maximum load of $400 \mu\text{N}$. Scale bar: $2 \mu\text{m}$. b) Mechanical behavior of the SRMs with 15 and 50 windings in LC mode tests at maximum applied load of 800 , 1600 , and $3200 \mu\text{N}$. Inset: SEM image revealing the damage of 15-winding SRM upon applying maximum load of $3200 \mu\text{N}$. Scale bar: $5 \mu\text{m}$. c) Creep behavior of 15- and 50-winding SRMs at maximum load of $400 \mu\text{N}$. d–f) Fatigue deformation of compact SRMs with 15 and 50 windings over 650 and 50 cycles, respectively, in the load range from 50 – $400 \mu\text{N}$. All the microtubes are made of Ti (15 nm)/Cr (20 nm) and released from a thin FC layer. The inner diameter of the microtubes D_{inn} is $\approx 3 \mu\text{m}$.

We simulated the mechanical behavior of the compact microtubes with different N_w of 2, 5, 10, 15, 20, 25, and 50 to understand the impact of N_w (t_{wall}) on their mechanical behavior. The geometry of a compact microtube with $t_{\text{wall}} = 0.07 \mu\text{m}$, which is equivalent to $N_w = 2$ and $D_{\text{inn}} = 3 \mu\text{m}$, is shown in **Figure 3a**. The microtube is deformed with a $5 \mu\text{m}$ flat cylindrical indenter, while the whole microtube is placed over a rigid substrate. Comparison of the results including the deformation behavior, stress, and strain distribution for the microtubes with $N_w = 2, 10, 25,$ and 50 is shown in **Figure 3b**. The contour plots reveal

how the mechanical stability of the microtubes increases when N_w (t_{wall}) increases from 2 to 50. While the two-winding microtube is permanently damaged with a small indentation load of $120 \mu\text{N}$, the microtube with 50 windings remains completely undamaged even when it is subjected to a load of $1800 \mu\text{N}$. The thick-walled microtube ($N_w = 50$) does not experience any plastic deformation compared with the thin-walled one ($N_w = 2$) with a large amount of plastic deformation.

The load–displacement curves for the compact microtubes with different N_w ranging from 2 to 50 are shown in

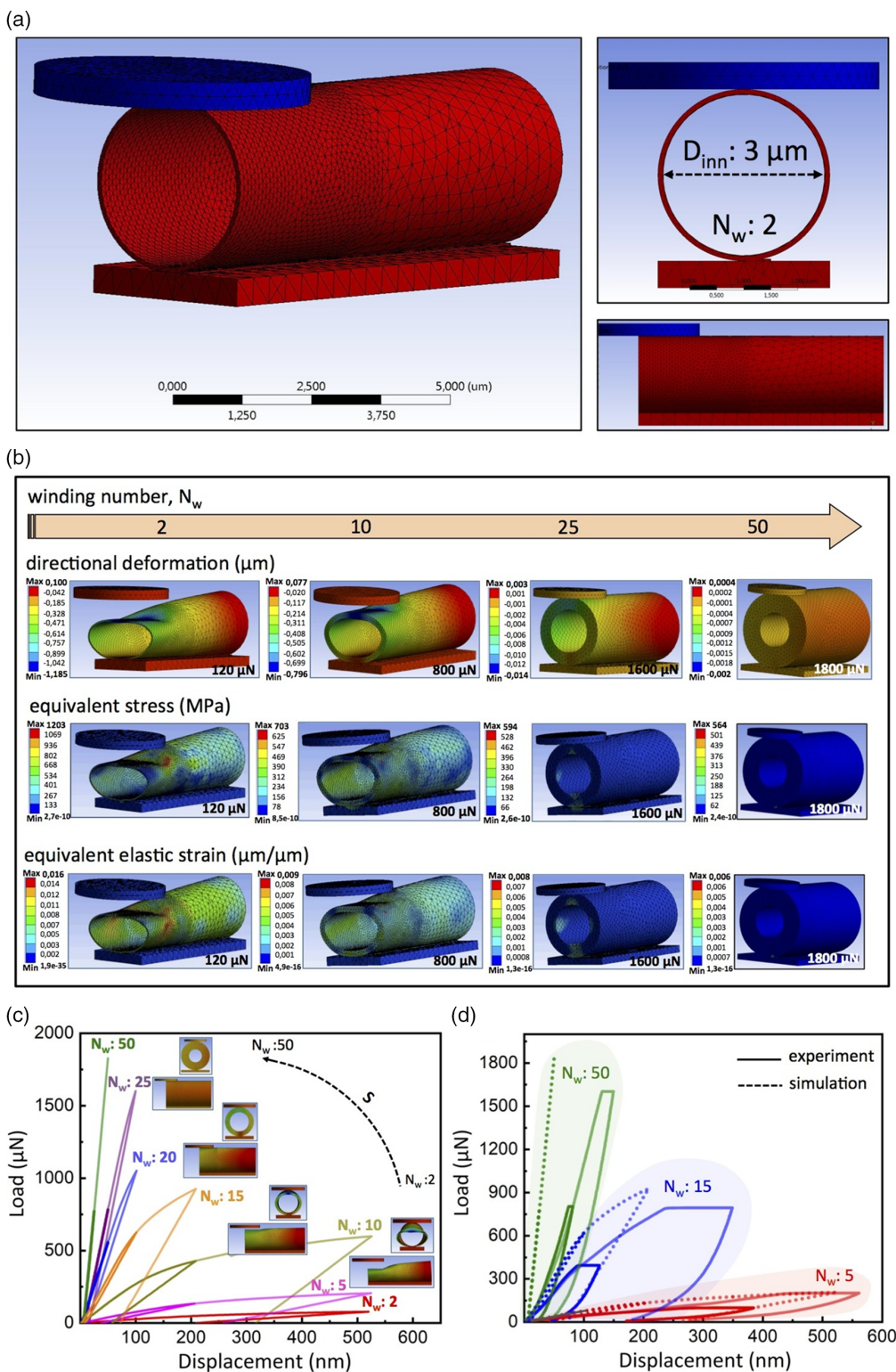


Figure 3. Simulation analysis on effect of windings number on the mechanical behavior of SRMs. a) Geometry detail of a microtube with N_w of 2 (wall thickness, t_w , of $0.07 \mu\text{m}$) and D_{inn} of $3 \mu\text{m}$. The load is applied by a $5 \mu\text{m}$ diameter flat cylindrical object. b) Comparison of the mechanical behavior of the compact microtubes with different N_w . Deformation behavior, distribution of stress and strain in the microtubes with 2, 10, 25, and 50 windings at maximum loads of 120, 800, 1600, and 1800 μN , respectively. c) Comparison of the load–displacement curves for the compact microtubes with different N_w ranging from 2 to 50. d) Comparison of the load–displacement plots for the SRMs and simulated microtubes with 5, 15, and 50 windings.

Figure 3c. The curves clearly demonstrate stiffness of the microtube; S increases dramatically as the winding number increases. The microtube with two windings, which has the thinnest wall, exhibits the lowest stiffness, while the 50-turn microtube, as the thickest one, is the most mechanically stable microtube. The stiffness changes by a factor of ≈ 80 from $\approx 0.5 \text{ kN m}^{-1}$ ($N_w = 2$) to $\approx 40 \text{ kN m}^{-1}$ ($N_w = 50$).

We compared the results from the FEA with experimental data. The load–displacement curves of the simulated compact microtubes and SRMs with 5, 15, and 50 windings are shown in Figure 3d. Both experimental and FEA load–displacement curves follow similar trends as increasing N_w causes the mechanical stability of the microtubes to increase. Quantitatively, there are some differences in the displacement magnitudes, which is due to the simplification in the models that do not consider the sliding of the windings as evident for the real rolled-up microtubes. Moreover, the creep effect, which is clearly found in the experimental load–displacement curves, and the influence of the load rates have not been considered in FEA as the applied material does not include viscoelastic effects. Furthermore, based on the FIB/SEM and energy dispersive X-ray (EDX) analysis of the compact SRMs, the existence of the FC layer (partially or totally) within the SRM windings is confirmed. The presence of the flexible polymeric FC layer^[51] in the windings helps to increase the flexibility of the SRMs causing higher plastic deformation before breakage and improving the fatigue behavior of the SRMs.

This mechanical analysis provides an estimate for the maximum allowed forces in a pick-and-place process for SRMs. The results show that the maximum applied force strongly depends on the number of windings (wall thickness) of the SRM. To prevent any excessive force exceeding fracture strength of the SRM, position and travel distance of the nozzle should be accurately programmed. For instance, for a thin SRM (N_w of 5) the pick-and-place force should be kept below $\approx 200 \mu\text{N}$ to avoid mechanical damages, while the thick SRM (N_w of 50) can withstand forces as high as $\approx 3200 \mu\text{N}$.

5.2. Effect of Winding Compactness

To evaluate the impact of the winding compactness on the mechanical behavior, we prepared noncompact bilayer SRMs as control structures (see Experimental Section) and compared their mechanical deformation with compact SRMs possessing the same N_w (15) and D_{inn} ($\approx 3 \mu\text{m}$). Figure 4a shows the typical load–displacement curves obtained in LC mode for different applied forces of 100, 200, and 400 μN for the noncompact and compact SRMs. SEM images (Figure 4a insets) reveal the tightness of the windings in these SRMs. Regardless of the winding number, SRMs with high compactness exhibit much higher mechanical stability under different loading conditions. While the compact SRM is completely stable at even 400 μN peak load, the noncompact SRM exhibits severe plastic deformation already at a low applied force of 100 μN . The pop-ins, which are observed during the loading sequence of the noncompact SRM, are caused by sudden displacements due to the spaces between consecutive windings or the result of breakages within individual windings. The presence of many separated thin windings due to a large

number of interfacial defects in the noncompact SRM provides less resistance to deformation upon loading. The presence of large spaces between the windings (voids) can cause the collapse of the individual windings even under low loading conditions. However, narrow gaps between adjacent windings are not critical as they vanished at low loading rates and as a result resistance to deformation increases. The correlation between the occurrence of pop-ins in the loading part of the load–displacement curve and the emergence of plastic damage in the SRMs windings has been analyzed and presented in Figure S2 and Movie S1, Supporting Information.

We also simulated the effect of compactness on the mechanical behavior of the microtubes by FEA. For this purpose, we designed a noncompact microtube with $D_{\text{inn}} = 3 \mu\text{m}$ and $N_w = 15$ ($t_{\text{wall}} = 0.525 \mu\text{m}$), which includes winding interfacial defects (two voids) in the upper part of the microtube beneath the indenter tip. The geometry details of this microtube are shown in Figure 4b. Similar to the compact microtube, the indentation process was done with a 5 μm diameter flat cylindrical object. The deformation behavior of the microtube as well as stress and strain relations upon loading and unloading is shown in Figure 4c. The deformation plots display how the windings (B_w) separated by the voids are compressed and irreversibly deform upon applying the indentation load. Stress concentration beneath the indenter tip and especially around the indenter edges can be detected. Contour plots reveal plastic deformation in the thin layers beneath the indenter tip after removal of the load.

The load–displacement curves of the simulated noncompact microtubes “see” two voids, as shown in Figure 4d. The slope of the loading part of the curve locally changes as the indentation load increases. These changes are related to the compression of the thin separated B_w upon the indentation process. As displayed in the upper left inset of the graph (Figure 4d), by inserting two interfacial defects between the windings three discrete B_w s are created in the microtube wall. By increasing the applied load, the space between the B_w s beneath the indenter tip completely vanishes and the windings get in contact. Consequently, thicker winding groups with higher deformation resistance are formed which cause the slope of the loading part of the curve to become steeper.

We compared both mechanical behaviors achieved in simulations and experiments for microtubes with different compactness, as shown in Figure 4e. The load–displacement curves for the compact and noncompact microtubes both with $N_w = 15$ and $D_{\text{inn}} = 3 \mu\text{m}$ demonstrate higher mechanical stiffness for the compact microtubes compared with the noncompact ones. The shapes of the loading parts of the load–displacement curves are quite different. In contrast to the noncompact microtubes, the loading part of the curve for the compact microtube has a regular and uniform shape without any noticeable indentation events. The noncompact microtube deforms up to $\approx 875 \text{ nm}$ when indented with a load of 600 μN , while the compact one experiences only $\approx 95 \text{ nm}$ deformation when the same indentation load is applied. Moreover, there are strong differences in the amount of plastic deformation between these two classes of microtubes. The noncompact microtube experiences a plastic deformation of $\approx 72\%$ upon applying a maximum load of 670 μN compared with the compact microtube with

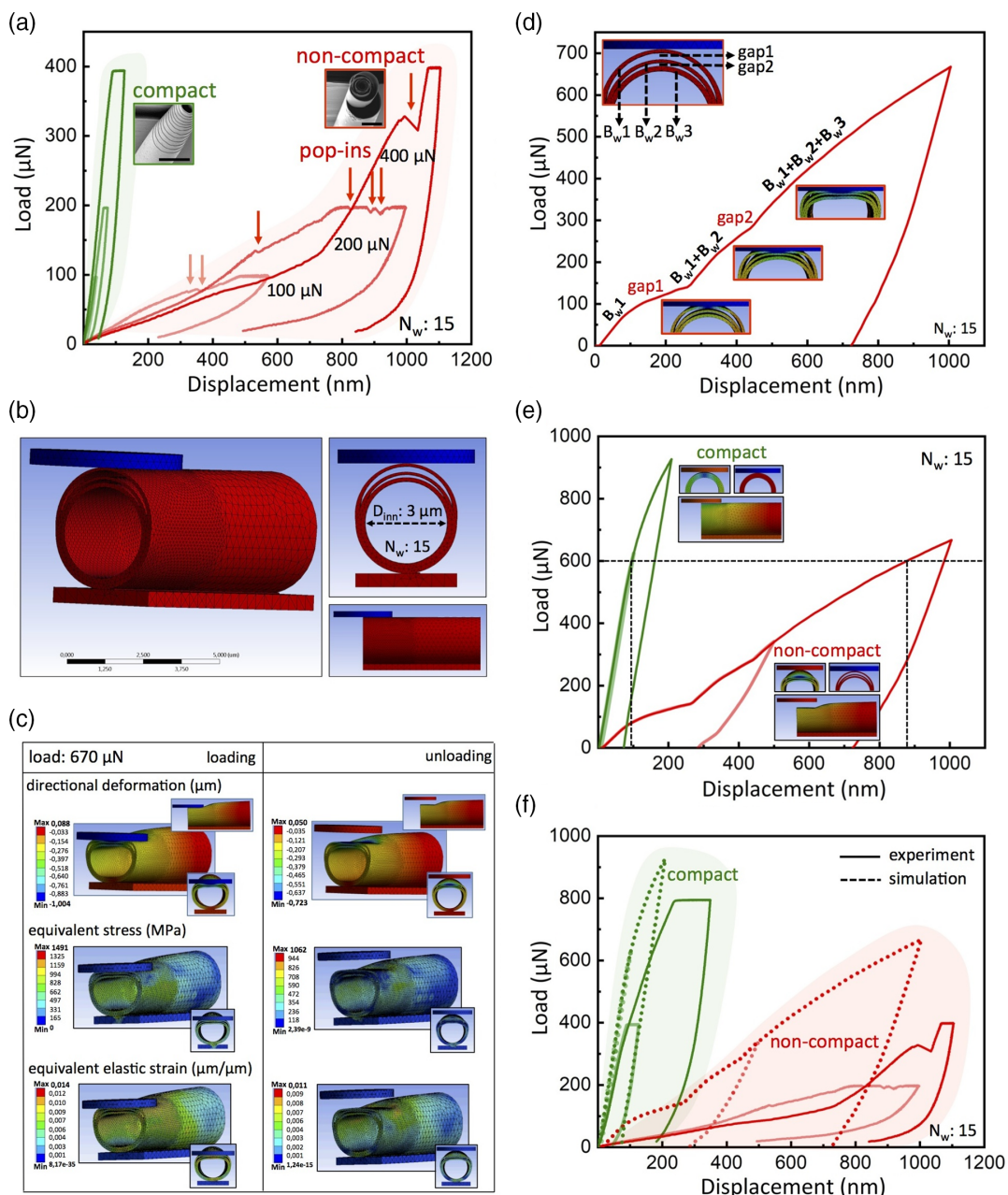


Figure 4. Effect of windings compactness level on the mechanical behavior of SRMs. a) Comparison of the load–displacement curves obtained under LC mode at 100, 200, and 400 μN peak loads for the compact and noncompact SRMs with N_w of 15 and D_{inn} of $\approx 3 \mu\text{m}$. The microtubes are made of Ti (15 nm)/Cr (20 nm). The inset SEM images reveal the compactness quality of the SRMs. Scale bars are 5 μm . b) Geometry detail of a simulated noncompact microtube with two voids between the windings and D_{inn} of 3 μm . The total thickness of the wall is 0.525 μm , which is corresponded to 15 windings. c) Deformation behavior, distribution of stress and strain in the noncompact microtube upon applying peak load of 670 μN during loading and unloading steps. d) Simulated load–displacement behavior of the noncompact microtube with two voids and three bunches of winding, B_w . The contour plots of the deformed microtube display how B_w s are compressed to each other upon applying the indentation load. e) Comparison of the simulated load–displacement curves for the compact and noncompact microtubes with the same N_w of 15 and D_{inn} of 3 μm . f) Comparison of the load–displacement plots for the compact and noncompact simulated microtubes and SRMs.

$\approx 35\%$ irreversible deformation upon indentation with a load of 900 μN . The subtle effect of the void position on the mechanical deformation of a noncompact microtube is studied in Figure S3–S6, Supporting Information.

The load–displacement plots for the compact and noncompact SRMs, and simulated indentations are shown in Figure 4f. In both cases, the noncompact microtubes have lower mechanical stiffness, higher irreversible deformation, and abnormal

load–displacement curves compared with the compact ones. In both simulations and experiments, the presence of the defects between windings results in local changes in the slope during the loading parts of the load–displacement curves. However, regardless of the creep, load rate effects, and the possible sliding of windings, the shape of the experimental and simulated curves does not fully match, which we attribute to a different number, kind, and distribution of the interwinding defects between the real structures and the FEA model.

The winding compactness of SRMs can drastically affect the maximum critical forces allowed for the pick-and-place process. The noncompact SRMs can easily break even if handled with a low pick-and-place force of 100 μN , compared with the ultracompact 15 winding SRMs, which can withstand forces up to 1.6 mN. An accurate adjustment of the nozzle pressure and movement is challenging when manipulating noncompact SRMs required to minimize SRM component cracking, as the number, kind, and distribution pattern of the interwinding defects is not known and can vary drastically from structure to structure. Precise control of pick-and-place nozzle pressure can be, however, precisely controlled based only on the knowledge of the wall thickness and diameter of compact SRMs.

5.3. Effect of Inner Diameter

The mechanical behavior of SRMs is also influenced by the inner diameter of the microtube, D_{inn} . According to the Timoshenko formula,^[52] the bending curvature of a bilayer system can be controlled by Young's modulus, initial thickness, and misfit strain of the deposited layers. Based on the results of our previous work,^[40] we found that the inner diameter of the SRM can be easily tuned by the initial thickness of the stained nanomembrane. To analyze the effect of this geometrical factor, SRMs with $D_{\text{inn}} = \approx 11 \mu\text{m}$ were prepared using a thicker nanomembrane and compared with bilayer SRMs with $D_{\text{inn}} = \approx 3 \mu\text{m}$ (see Experimental Section for fabrication details). The SRMs with the large inner diameter ($D_{\text{inn}} = \approx 11$) possessing different number of windings of 5 and 15 were indented under LC conditions reaching various maximum loads ranging from 100 to 800 μN . Mechanical responses of SRMs in terms of N_w at the maximum load of 800 μN are shown in **Figure 5a**. The five-winding SRM was mechanically fragile and partially broke at this loading condition in contrast to the 15-winding SRM, which shows a normal load–displacement curve, indicating its high mechanical stability. The pop-ins appearing in the load part of the curve signify a permanent mechanical damage in the five-winding SRM. However, the SEM images shown in **Figure 5b** for the large and compact five-winding SRM loaded up to a maximum force of 600 μN reveal that the large deformation upon applying the load can be recovered without considerable permanent deformation or structural collapse after removing the force. Although a microscopic analysis of the outer surface of the SRM after the nanoindentation revealed no permanent mechanical damages such as cracks or even sensible changes in the circularity of the SRM, the presence of a pop-out event^[45,53] in the load–displacement curve during the unloading process and some irregularities in the shape of the loading part can be attributed to some slight plastic deformation inside the SRM

(**Figure 5c**). The local deformation at the contact interface of the compact five-winding SRM and the indenter tip upon loading is shown in more detail in **Figure S7**, **Movie S2**, **S3**, **Supporting Information**.

The difference of the load–displacement curves for the SRMs with $D_{\text{inn}} = \approx 3$ and $\approx 11 \mu\text{m}$ with the same N_w of 15 at various maximum loads of 200, 400, and 800 μN is shown in **Figure 5d**. The comparison shows that the penetration depth under the same loading condition for the SRM with larger D_{inn} of $\approx 11 \mu\text{m}$ is around ten times larger than for the SRM with D_{inn} of $\approx 3 \mu\text{m}$, which proves higher mechanical stiffness of the small SRM. These findings indicate that the mechanical behavior of the SRMs is following the “smaller is stronger” phenomena as the deformation stiffness is higher for the SRMs with smaller diameter.^[54]

We also investigated the diameter effect by performing FEA. We designed a microtube with a large D_{inn} of 11 μm and t_{wall} of 0.525 μm , which is equivalent to the wall thickness of a 15-winding bilayer microtube. The simulated large diameter microtubes were indented under the same conditions as the small diameter microtubes. **Figure 5e** shows the geometry details of the designed microtube. The deformation contour plots and stress and strain distribution upon applying the peak load of 430 μN during the loading and unloading steps are shown in **Figure 5f**. These results confirm that there is no plastic deformation after removal of the load and the large diameter microtube has experienced only the elastic strain under the indentation process.

The mechanical behavior of the simulated microtubes with $D_{\text{inn}} = 3$ and 11 μm is shown in **Figure 5g**. The load–displacement curves reveal that the microtube with small D_{inn} is much stiffer than the microtube with large D_{inn} , which is consistent with the experimental results. The small diameter microtube deformed only up to $\approx 60 \text{ nm}$ at the load of 400 μN , while the large diameter microtube experienced an indentation depth of $\approx 550 \text{ nm}$ upon the same indentation load. The small diameter microtube has a stiffness of $\approx 6.7 \text{ kN m}^{-1}$, which is around ≈ 9 times stiffer than the large diameter microtube with a stiffness of $\approx 730 \text{ N m}^{-1}$.

The load–displacement curves for the experimental SRMs and simulated microtubes are shown in **Figure 5h**. The same trend can be found for both the computational study and the experimental data regarding the effect of D_{inn} on mechanical deformation of the microtubes. In both cases, increasing D_{inn} in the microtube results in a lower mechanical stiffness. However, as already pointed out, some assumptions made for the simulation analysis lead to a mismatch for the shape of the load–displacement curves between the simulated and experimental results.

Concerning the pick-and-place operation, although the bigger diameter SRM ($D_{\text{inn}} = 11 \mu\text{m}$) is less stiff than the small diameter one ($D_{\text{inn}} = 3 \mu\text{m}$) and undergoes much larger deformations, the deformation is mostly elastic and can be recovered after the 3D device is placed on a microchip or a PCB without considerable damage. Our studies reveal that more precise alignment of the pick-and-place nozzle is required for operation on smaller SRMs, which is more challenging than operations with bigger SRMs. This may require a longer grasping time for the smaller SRMs.

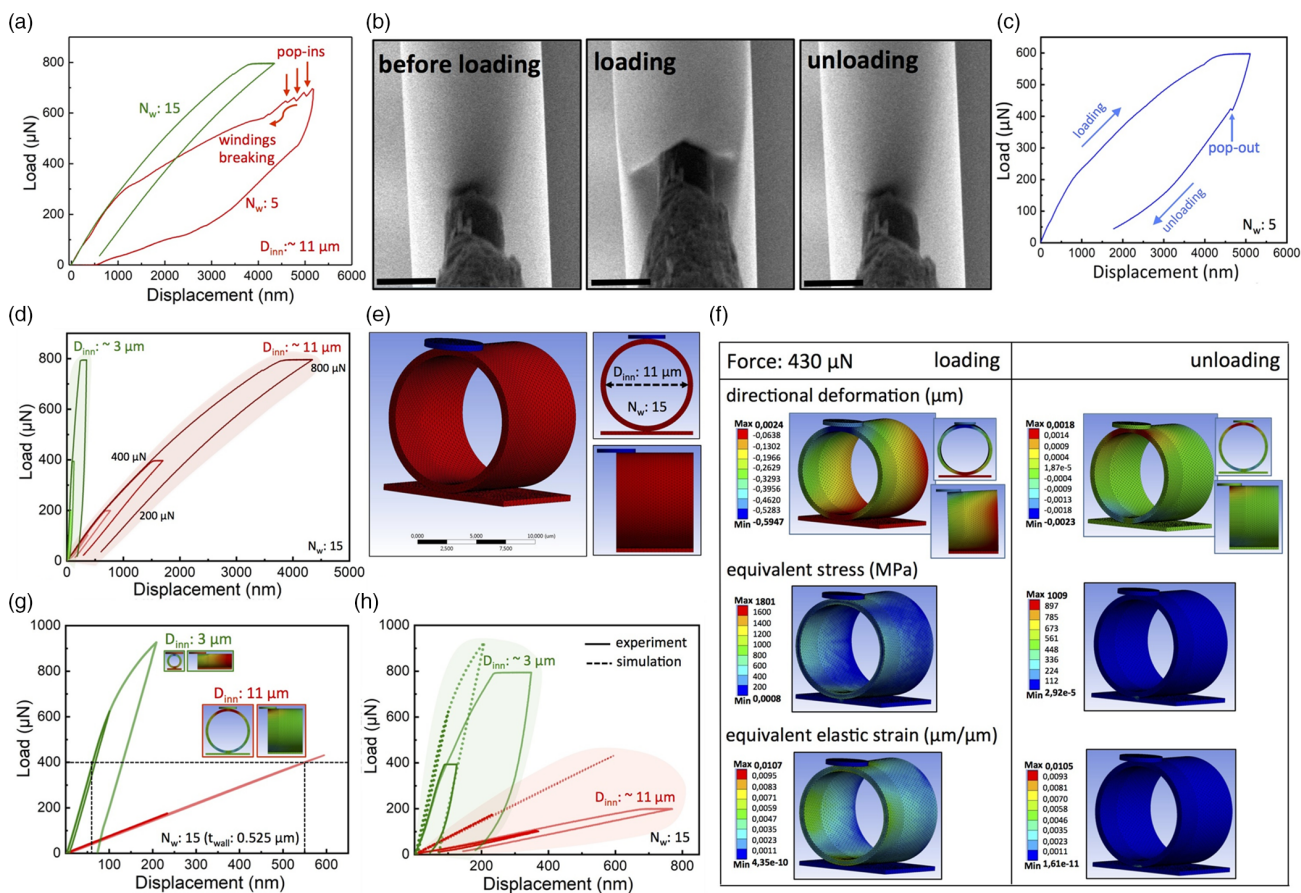


Figure 5. Effect of inner diameter on the mechanical behavior of SRMs. a) Load–displacement curves for the compact SRMs with D_{inn} of $\approx 11 \mu\text{m}$ and N_w of 5 and 15 at maximum load of $800 \mu\text{N}$ under LC mode tests. b) SEM images show the sequence of deformation response of the five-winding SRM at maximum load of $600 \mu\text{N}$. Scale bars are $5 \mu\text{m}$. c) Load–displacement curve for the compact five-winding SRM upon applying maximum load of $600 \mu\text{N}$ which reveals a pop-out event in the unloading step. d) Comparison of the load–displacement curves for the compact SRMs with D_{inn} of ≈ 3 and $\approx 11 \mu\text{m}$ at various pick loads. e) Geometry detail of a microtube with D_{inn} of $11 \mu\text{m}$ and N_w of 15. f) Deformation behavior, distribution of stress and strain in the microtube upon applying maximum load of $430 \mu\text{N}$ during loading and unloading steps. g) Simulated load–displacement curves for the compact microtubes with D_{inn} of 3 and $11 \mu\text{m}$. h) Comparison of the load–displacement plots for the compact SRMs and simulated microtubes with D_{inn} of 3 and $11 \mu\text{m}$.

6. Conclusion

We have investigated the mechanical behavior of compact SRMs fabricated by a dry rolling technique using an in situ SEM nanoindentation system equipped with a flat cylindrical punch tip. Our experiments mimic loading conditions present in, i.e., a pick-and-place process required for final application of microscale discrete passive electronic components. Accurate load–displacement measurements and complete observation of the deformed SRMs inside SEM enabled us to detect the real-time deformation of the SRMs upon loading and removal of the load. Mechanical characterization of the SRMs under different loading conditions with different loading rates, creep, and cyclic loading was conducted. We found that the mechanical deformation response of multiwinding SRMs can be controlled by three geometric parameters, including the number of windings, compactness of consecutive windings, and inner diameter of the microtube. Increasing the microtube winding number leads to higher stiffness. The SRM stiffness increased from

≈ 1.8 to $\approx 33 \text{ kN m}^{-1}$ when the number of windings increased from 5 to 50. We also observed that thicker walled SRMs exhibit less creep under the same load indentation. The maximum penetration depth per cycle of thicker walled SRM was lower than those of thinner walled SRM, suggesting that thicker walled SRMs have higher cyclic penetration resistance. We demonstrated that the tightness between neighboring windings contributes significantly to the stability of the SRMs. Noncompact SRMs exhibited lower mechanical stiffness, higher irreversible deformation, and abnormal load–displacement curves compared with the compact ones. Indenting the SRMs with different inner diameters revealed that the smaller SRMs are mechanically stiffer than their large diameter counterparts. However, the large diameter SRMs showed excellent deformation recovery after the unloading process. Numerical FEA revealed the influence of the three geometrical parameters on the deformation behavior of the microtubes. All the simulation results were compared with the experimental data. The good agreement between the experimental results and the simulation analysis demonstrated the adequate

in situ mechanical characterizations of the SRMs using the nano-indentation system. Moreover, we can conclude that forces from hundreds of micro-Newton to a few milli-Newton depending on the wall thickness and inner diameter of the compact SRMs can be applied during the pick-and-place operation.

Thorough mechanical analysis presented here facilitates the development of novel head technologies for new pick-and-place equipment compatible with high-volume manufacturing using 3D self-assembled components. The new head techniques must be capable of safe handling of these irregular-shaped SRMs structures and consider unwanted adhesive forces dominant at microscales during detachment and placement steps. Furthermore, accurate vacuum measurement and high-resolution vision systems will be necessary to detect these tiny structures.

7. Experimental Section

Preparation of FC Layer: Silicon substrate was first cleaned by immersion in DMSO, acetone, and isopropanol. The process was followed by O₂-plasma etching step for removal of residuals from the surface of the substrate. The FC layer was dip coated on silicon substrate by immersion in bath of a fluropolymers solution (3M Novec 1700 Electronic Grade Coating). Afterward, the FC-coated substrate was heated at 100 °C for a minute to evaporate the extra solvent. Different FC solution concentrations can be prepared by means of a FC-based solvent (3M Novec Engineered Fluid 7100).

Photolithographic Patterning of Strained Nanomembrane on FC Layer: To improve the adhesion of the FC layer onto the substrate during the patterning process, first a monolayer of Ti-Prime was spin-coated at 3500 rpm for 20 s. After coating the FC layer and prior to photoresist processing, a second layer of Ti-Prime was spin-coated on the FC layer to guarantee good uniformity of the photoresist on the FC layer. Afterward, AZ5214E photoresist (MicroChem) was spin-coated on the FC layer at 4500 rpm for 35 s and then was baked for 5 min at 90 °C on a hot plate. The exposure step was done using µPG 501 maskless aligner system (Heidelberg). After postbaking process for 2 min at 120 °C, flood illumination for 30 s was done by a MJB4 mask aligner system (SUSS MicroTec). The development process was done in AZ 726 MIF (MicroChem) for 45 s. After deposition of the strained nanomembrane, lift-off process was done in an ultrasonic bath of concentrated aqueous-alkaline AR 300-35 developer (Allresist) for several minutes.

Fabrication of Small D_{inn} SRMs: The strained bilayer nanomembrane consisting of Ti (15 nm)/Cr (20 nm) was deposited in an e-beam evaporator (IM9912-Micronova). The deposition rates of 2.5 and 3 Å s⁻¹ for Ti and Cr were set, respectively. To prevent the crack formation during the deposition, the temperature inside the evaporator was kept below 60 °C. For the compact microtubes, a thin FC layer (thickness of ≈40 nm) was used to detach and roll up the bilayer upon heat treatment at 160 °C on a hotplate. To prepare the noncompact SRM, the bilayer nanomembrane of Ti (15 nm)/Cr (20 nm) was released by a thick FC layer (≈100 nm). The compactness level of the SRM windings can be controlled by the FC layer thickness.

Fabrication of Large D_{inn} SRMs: The inner diameter of the SRMs can be tuned by the initial thickness of the nanomembrane. The thick multilayer nanomembrane consisting of Ti (15 nm)/Cr (20 nm)/Al₂O₃ (10 nm)/Cr (30 nm)/Al₂O₃ (10 nm) with the total layer thickness of 85 nm was rolled up by a thin FC layer (≈40 nm) upon thermal annealing at 160 °C on a typical hotplate. The metallic layers of Ti and Cr were evaporated at the low temperature (<60 °C) and deposition rates of 2.5 and 3 Å s⁻¹, respectively. Al₂O₃ layers were deposited by atomic layer deposition (ALD) at 80 °C with the rate of 1.1 Å per cycle (SavannahTM 100, Cambridge NanoTech Inc.).

Cross-Sectional Characterization of SRMs: The images of the fabricated SRMs were prepared by means of a SEM (NVision 40 CrossBeam, Carl Zeiss). The acceleration voltage was 2–5 kV. For the cross-sectional

images, an attached Ga-ion FIB milling column for vertical cutting was used (Zeiss NVision40 dual-beam).

Mechanical Characterization: All the mechanical characterization experiments were performed using an in situ SEM (Zeiss Auriga CrossBeam 40) nanoindentation system (Bruker Nanoindenter PI88) equipped with a 5 µm diameter flat cylindrical punch diamond tip. Before each measurement the displacement drift was measured over a time of 30 s and only if the drift was below 0.5 nm s⁻¹ and did not change significantly over time, the actual measurement was performed. Using the obtained displacement drift, all the measured data were corrected.

FEA: The simulation analysis was conducted using ANSYS software (version 17.2 Academics). The compact microtube was assumed to be a typical hollow cylindrical structure. The metal plasticity model of bilinear isotropic and the titanium alloy as the material of the microtube were selected. Materials data used for the simulation of the microtubes were Young's modulus of 96 GPa, Poisson ratio of 0.36, yield strength of 930 MPa, tangent modulus of 2150 MPa, and shear modulus of 35.3 GPa. The microtubes were indented vertically by a 5 µm diameter flat cylindrical object. Directional deformation in Y direction, equivalent von Mises stress, and equivalent elastic strain in the solid microtube were measured. Depending on the microtube wall thickness (t_{wall}) and the inner diameter of the microtube (D_{inn}), various displacements from 0.05 to 1 µm were applied.

Supporting Information

Supporting Information is available from the Wiley Online Library or from the author.

Acknowledgements

The authors thank Paul Plocica for technical help, Stefan Baunack for FIB/SEM analysis, and Ulrike Nitzsche for help with the calculation server. This work was financially supported by the International Research Training Group (IRTG) project GRK 1215 "Materials and Concepts for Advanced Interconnects and Nanosystems." O.G.S. acknowledges financial support by the Leibniz Program of the German Research Foundation (SCHM 1298/26-1). D.K. acknowledges financial support by the German Research Foundation DFG (KA5051/1-1).

Open access funding enabled and organized by Projekt DEAL.

Conflict of Interest

The authors declare no conflict of interest.

Data Availability Statement

Data available on request from the authors.

Keywords

mechanical deformation, nanoindentation, simulation analysis., Swiss-roll microstructures, winding compactness

Received: May 4, 2021
Published online: May 28, 2021

- [1] A. Piqué, P. Serra, in *Laser Printing of Functional Materials: 3D Microfabrication, Electronics and Biomedicine*, Wiley-VCH Verlag GmbH & Co. KGaA, Weinheim, Germany 2018.
- [2] D. Karnausenko, T. Kang, V. K. Bandari, F. Zhu, O. G. Schmidt, *Adv. Mater.* 2020, 32, 1902994

- [3] A. N. Das, R. Murthy, D. O. Popa, H. E. Stephanou, *IEEE Trans. Autom. Sci. Eng.* **2012**, 9, 160.
- [4] W. J. Plumbridge, R. J. Matela, A. Westwater, in *Structural Integrity and Reliability in Electronics: Enhancing Performance in A Lead-Free Environment*, Springer, Netherlands **2004**.
- [5] O. G. Schmidt, K. Eberl, *Nature* **2001**, 410, 168.
- [6] V. Y. Prinz, V. A. Seleznev, A. K. Gutakovsky, A. V. Chehovskiy, V. V. Preobrazhenskii, M. A. Putyato, T. A. Gavrilova, *Phys. E* **2000**, 6, 828.
- [7] O. G. Schmidt, N. Schmarje, C. Deneke, C. Müller, N. Y. Jin-Phillipp, *Adv. Mater.* **2001**, 13, 756.
- [8] D. Karnaushenko, T. Kang, O. G. Schmidt, *Adv. Mater. Technol.* **2019**, 4, 1800692.
- [9] J. Rogers, Y. Huang, O. G. Schmidt, D. H. Gracias, *MRS Bull.* **2016**, 41, 123.
- [10] C. C. Bof Bufon, J. D. Cojal González, D. J. Thurmer, D. Grimm, M. Bauer, O. G. Schmidt, *Nano Lett.* **2010**, 10, 2506.
- [11] R. Sharma, C. C. B. Bufon, D. Grimm, R. Sommer, A. Wollatz, J. Schadewald, D. J. Thurmer, P. F. Siles, M. Bauer, O. G. Schmidt, *Adv. Energy Mater.* **2014**, 4, 1301631.
- [12] F. Gabler, D. D. Karnaushenko, D. Karnaushenko, O. G. Schmidt, *Nat. Commun.* **2019**, 10, 3013.
- [13] F. Gabler, O. G. Schmidt, *IEEE Trans. Compon. Packag. Manuf. Technol.* **2020**, 10, 1251.
- [14] C. N. Saggau, F. Gabler, D. D. Karnaushenko, D. Karnaushenko, L. Ma, O. G. Schmidt, *Adv. Mater.* **2020**, 2003252.
- [15] W. Huang, Z. Yang, M. D. Kraman, Q. Wang, Z. Ou, M. Muñoz Rojo, A. S. Yalamarthi, V. Chen, F. Lian, J. H. Ni, S. Liu, H. Yu, L. Sang, J. Michaels, D. J. Sievers, J. G. Eden, P. V. Braun, Q. Chen, S. Gong, D. G. Senesky, E. Pop, X. Li, *Sci. Adv.* **2020**, 6, eaay4508.
- [16] D. D. Karnaushenko, D. Karnaushenko, H.-J. Grafe, V. Kataev, B. Büchner, O. G. Schmidt, *Adv. Electron. Mater.* **2018**, 4, 1800298.
- [17] X. Yu, W. Huang, M. Li, T. M. Comberiate, S. Gong, J. E. Schutt-Aine, X. Li, *Sci. Rep.* **2015**, 5, 1.
- [18] W. Huang, X. Yu, P. Froeter, R. Xu, P. Ferreira, X. Li, *Nano Lett.* **2012**, 12, 6283.
- [19] W. Huang, J. Zhou, P. J. Froeter, K. Walsh, S. Liu, M. D. Kraman, M. Li, J. A. Michaels, D. J. Sievers, S. Gong, X. Li, *Nat. Electron.* **2018**, 1, 305.
- [20] D. Grimm, C. C. Bof Bufon, C. Deneke, P. Atkinson, D. J. Thurmer, F. Schäffel, S. Gorantla, A. Bachmattiuk, O. G. Schmidt, *Nano Lett.* **2013**, 13, 213.
- [21] T. Deng, Z. Zhang, Y. Liu, Y. Wang, F. Su, S. Li, Y. Zhang, H. Li, H. Chen, Z. Zhao, Y. Li, Z. Liu, *Nano Lett.* **2019**, 19, 1494.
- [22] K. Torikai, R. Furlan De Oliveira, D. H. Starnini De Camargo, C. C. Bof Bufon, *Nano Lett.* **2018**, 18, 5552.
- [23] B. Xu, Z. Tian, J. Wang, H. Han, T. Lee, Y. Mei, *Sci. Adv.* **2018**, 4, eaap8203.
- [24] H. Wang, H. Zhen, S. Li, Y. Jing, G. Huang, Y. Mei, W. Lu, *Sci. Adv.* **2016**, 2, el600027.
- [25] T. Li, V. K. Bandari, M. Hantusch, J. Xin, R. Kuhrt, R. Ravishankar, L. Xu, J. Zhang, M. Knupfer, F. Zhu, D. Yan, O. G. Schmidt, *Nat. Commun.* **2020**, 11, 3592.
- [26] D. D. Karnaushenko, D. Karnaushenko, D. Makarov, O. G. Schmidt, *NPG Asia Mater.* **2015**, 7, e188.
- [27] A. Fletcher. Restricted MLCC Supply Focuses on Re-Design Activity, **2018**, <https://www.electronicsspecifier.com/news/analysis/restricted-mlcc-supply-focuses-on-re-design-activity>.
- [28] P. Ming-Jen, C. A. Randall, *IEEE Electr. Insul. Mag.* **2010**, 26, 44.
- [29] W. Ho, P. Ji, P. K. Dey, *Int. J. Adv. Manuf. Tech.* **2008**, 37, 828.
- [30] M. Ayob, P. Cowling, G. Kendall, *Proc. IEEE Int. Conf. on Industrial Technology (IEEE ICIT '02)*, IEEE, Piscataway, NJ **2002**, p. 498.
- [31] K. Kallio, M. Johnsson, O. S. Nevalainen, *Eng. Res. Dev.* **2012**, 6, 319.
- [32] Z. Shook, *SMT Preventive Maintenance: Stop 5 Major Problems with Pick-and-Place Nozzles*, <http://smt.iconnect007.media/index.php/article/52613/smt-preventive-maintenance-stop-5-major-problems-with-pick-and-place-nozzles/52616/?skin=smt/>.
- [33] S. Qu, Y. Liu, *Wafer-Level Chip-Scale Packaging: Analog and Power Semiconductor Applications*, Springer-Verlag New York, USA **2015**, p. 227.
- [34] ESPOS Photonics Corporation, *APPLICATION NOTE-AN08: Assembly Process Guidelines*, ESPOS Photonics Corporation, Sargans, Switzerland **2020**.
- [35] Infineon Technologies AG, *General Recommendations for Assembly of Infineon Packages, Revision 4.0*, Infineon Technologies AG, Munich, Germany **2017**.
- [36] Juki Automation Systems AG, *Nozzle Application Catalogue*, Juki Automation Systems AG, Solothurn, Switzerland **2004**.
- [37] Y. Zhang, B. K. Chen, X. Liu, Y. Sun, *IEEE Trans. Robot.* **2010**, 26, 200.
- [38] L. Zhang, L. Dong, B. J. Nelson, *Appl. Phys. Lett.* **2008**, 92, 243102.
- [39] C. Müller, G. B. de Souza, A. Mikowski, O. G. Schmidt, C. M. Lepienski, D. H. Mosca, *J. Appl. Phys.* **2011**, 110, 044326.
- [40] S. Moradi, E. S. G. Naz, G. Li, N. Bandari, V. K. Bandari, F. Zhu, H. Wendrock, O. G. Schmidt, *Adv. Mater. Interfaces* **2020**, 7, 1902048.
- [41] C. A. Schuh, *Mater. Today*, **2006**, 9, 32.
- [42] S. J. Bull, *J. Phys. D: Appl. Phys.* **2005**, 38, 393.
- [43] U. Ramamurty, J. Jang, *CrystEngComm*, **2014**, 16, 12.
- [44] D. Maharaj, B. Bhushan, *beilstein J. Nanotechnol.* **2014**, 5, 822.
- [45] S. Wang, H. Liu, L. Xu, X. Du, D. Zhao, B. Zhu, M. Yu, H. Zhao, *Sci. Rep.* **2017**, 7, 8682.
- [46] Q. Guo, X. Fu, X. Guo, Z. Liu, Y. Shi, D. Zhang, *JOM*, **2018**, 70, 487.
- [47] S. V. Hainsworth, H. W. Chandler, T. F. Page, *J. Mater. Res.* **1996**, 11, 1987.
- [48] J. D. Nowak, K. A. Rzepiejewska-Malyska, R. C. Major, O. L. Warren, J. Michler, *Mater. Today*, **2009**, 12, 44.
- [49] V. Lyamkin, P. Starke, C. Boller, *7th Int. Symp. on Aircraft Materials (ACMA2018)*, Compiègne, France, 24–26 April **2018**.
- [50] D. Tischler, M. Válová, I. Štěpánek, *Acta Polytech. Hungarica* **2012**, 9, 167.
- [51] J. E. Lee, H. K. Kim, *Sci. Rep.* **2019**, 9, 16723.
- [52] S. Timoshenko, *J. Opt. Soc. Am.* **1925**, 11, 233.
- [53] L. Chang, L. C. Zhang, *Acta Mater.* **2009**, 57, 2148.
- [54] D. Maharaj, B. Bhushan, *Sci. Rep.* **2015**, 5, 8539.